Chemical Geology 617 (2023) 121243

Contents lists available at ScienceDirect

Chemical Geology

journal homepage: www.elsevier.com/locate/chemgeo

The Emeishan large igneous province eruption triggered coastal perturbations and the Capitanian mass extinction: Insights from mercury in Permian bauxite beds

Kunyue Ling [a], Hanjie Wen [b,c,*], Stephen E. Grasby [d], Haonan Zhao [a,e], Changzhou Deng [a], Runsheng Yin [a,*]

[a] State Key Laboratory of Ore Deposit Geochemistry, Institute of Geochemistry, Chinese Academy of Sciences, Guiyang 550081, China
[b] School of Earth Science and Resources, Chang'an University, Xi'an 710054, China
[c] College of Earth and Planetary Sciences, University of Chinese Academy of Sciences, Beijing 100049, China
[d] Geological Survey of Canada, Calgary Natural Resources Canada, 3303 33rd Street NW, Calgary, AB, T2L 2A7, Canada
[e] School of Earth Science and Engineering, Hebei University of Engineering, Handan 056038, China

ARTICLE INFO

Editor: Dr. Christian France-Lanord

Keywords:
Mercury
Emeishan large igneous province
Capitanian mass extinction
Bauxite bed

ABSTRACT

The Capitanian mass extinction occurring at the mid-Capitanian to the Guadalupian–Lopingian boundary (GLB; ca. 262–257 Ma) was temporally coincident with the eruption of the Emeishan large igneous province (LIP). Recent observation of Hg anomalies at the GLB at shelf and slope/basinal settings demonstrated a possible causal link between the Capitanian extinction and the Emeishan LIP eruption. However, Hg records of the GLB at coastal settings remain uninvestigated, limiting our knowledge of global impact of the Emeishan LIP and its role in the Capitanian mass extinction. Here we report new datasets of Hg concentrations, Hg isotopes and organic carbon isotopes in two coastal shallow-water sections in the Guangxi region, SW China. Elevated Hg/TOC ratios (up to 3330 and 221 ppb/wt%, respectively) and near-zero to positive Δ^{199}Hg values (−0.04‰ to +0.26‰) were observed across the GLB in the two sections, indicative of extensive volcanic Hg input to the ocean via wet Hg(II) deposition. A negative $\delta^{13}C_{org}$ excursion (2.5‰) coincides with widespread marine anoxia, peak Emeishan LIP magmatism, Hg/TOC anomalies, sea-level rise, and the Capitanian mass extinction. The temporal link between these phenomena suggests that the Emeishan LIP was a key driver of the climate/ocean dynamics, global ecosystems, and the formation of bauxite beds during the GLB.

1. Introduction

The Capitanian mass extinction occurring at the mid-Capitanian to the Guadalupan–Lopingian boundary (GLB; ca. 262–259 Ma) was a severe biotic crisis in the Phanerozoic (Jin et al., 2006; Huang et al., 2019; Bond et al., 2020). Fossil records indicate that this crisis affected shallow-marine taxa (e.g., corals, fusulinacean foraminifera, brachiopods, bivalves, and ammonoids), and terrestrial taxa (e.g., dinocephalian reptiles, vertebrates, and floral communities), to a large extent, but its cause is enigmatic (Retallack et al., 2006; Bond et al., 2010; Stevens et al., 2011). Ocean anoxia (Bond et al., 2015), global cooling (Isozaki, 2007), and global changes triggered by large volcanism such as death-by-photosynthetic shutdown at the onset of volcanism (Bond et al., 2010), ocean acidification caused by volcanogenic CO_2 (McGhee et al., 2013), and volcanogenic toxic metal poisoning (Grasby et al., 2016), are possible mechanisms of the Capitanian extinction.

Mercury (Hg) can trace large volcanism in geologic history (Grasby et al., 2019). Volcanism emits large amounts of Hg to the atmosphere, which has a long atmospheric residence time (~1 year) and can be transported globally prior to being deposited on land and ocean systems via wet and dry deposition pathways. Large igneous province (LIP) eruptions can result in transient emission of massive amounts of Hg, leading to anomalously high Hg concentrations in global sediments (Blum et al., 2014; Grasby et al., 2020). Given that organic matter (OM) has a strong affinity for Hg, anomalously high Hg to total organic carbon (Hg/TOC) ratios can better reveal large volcanisms in the geological record (Grasby et al., 2019).

Mercury isotopes undergo both mass-dependent fractionation (MDF;

* Corresponding authors.
E-mail addresses: wenhanjie@vip.gyig.ac.cn (H. Wen), yinrunsheng@mail.gyig.ac.cn (R. Yin).

https://doi.org/10.1016/j.chemgeo.2022.121243
Received 13 June 2022; Received in revised form 25 November 2022; Accepted 28 November 2022
Available online 30 November 2022

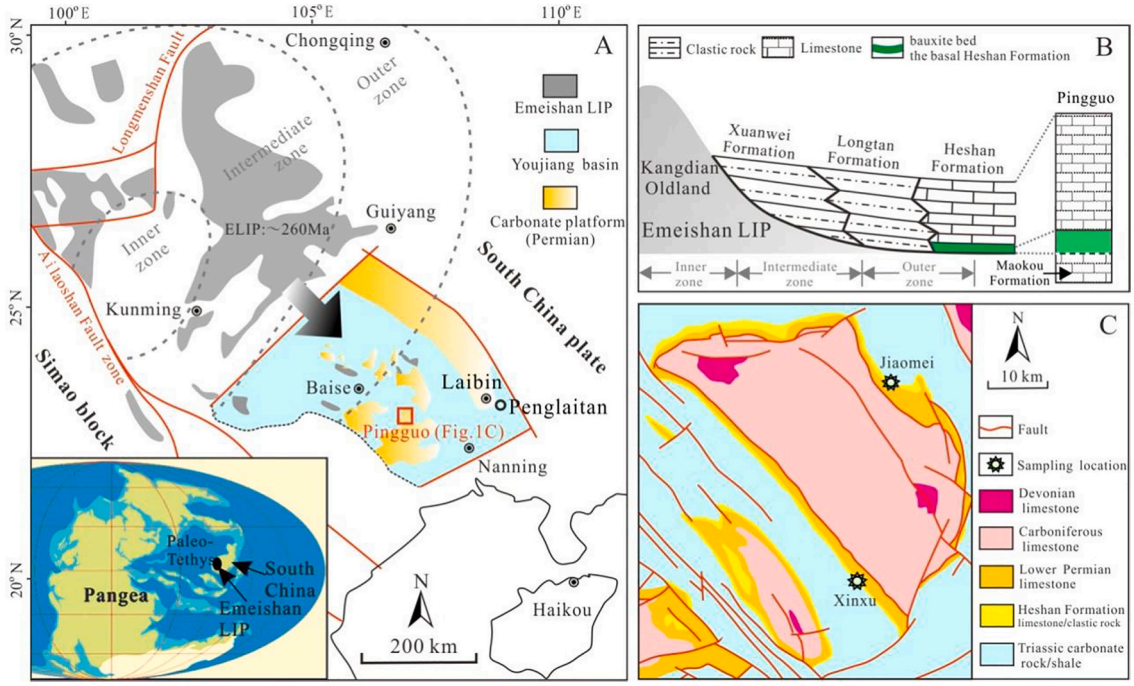

Fig. 1. (A) Simplified tectonic map of the southwestern Yangtze Craton and middle–late Permian palaeogeography of the Youjiang Basin (modified from He et al., 2003 and Yu et al., 2019). (B) Palaeogeographic map for the period after the formation of the Emeishan LIP, showing the location of the basal Heshan Formation bauxite bed (modified from He et al., 2003). (C) Geological map of the Pingguo area, Guangxi region, SW China.

reported in δ^{202}Hg) and mass-independent fractionation (MIF; reported in Δ^{199}Hg). MDF occurs during various physical, chemical, and biological processes, while MIF occurs mainly via photochemical processes with little interference from other processes and can provide unambiguous source constraints (Blum et al., 2014; Yin et al., 2022). Volcanic Hg related to the primitive mantle usually has near-zero MIF signals (Δ^{199}Hg ≈ 0, Zambardi et al., 2009; Moynier et al., 2021), but can be modified by Hg(II) photoreduction process on Earth's surface, resulting in negative Δ^{199}Hg values in terrestrial systems (e.g., soil and vegetation) and positive Δ^{199}Hg values in marine systems (e.g., seawater and sediments) (Blum et al., 2014). Recent studies have reported Hg (or Hg/TOC) anomalies with significant Δ^{199}Hg shifts during the Cryogenian interglacial greenhouse (Zhou et al., 2021), Ordovician-Silurian mass extinction (Gong et al., 2017), end-Permian mass extinction (Grasby et al., 2017, 2021; Shen et al., 2019a; Wang et al., 2021), and the T-J boundary mass extinction (Thibodeau et al., 2016; Shen et al., 2022), highlighting large volcanism as drivers of these events.

Significant Hg anomalies have been documented around the GLB in shelf settings in Spitsbergen, Europe, Borup Fiord in Canada, and basin/slope settings (Penglaitan) in SW China (Grasby et al., 2016; Huang

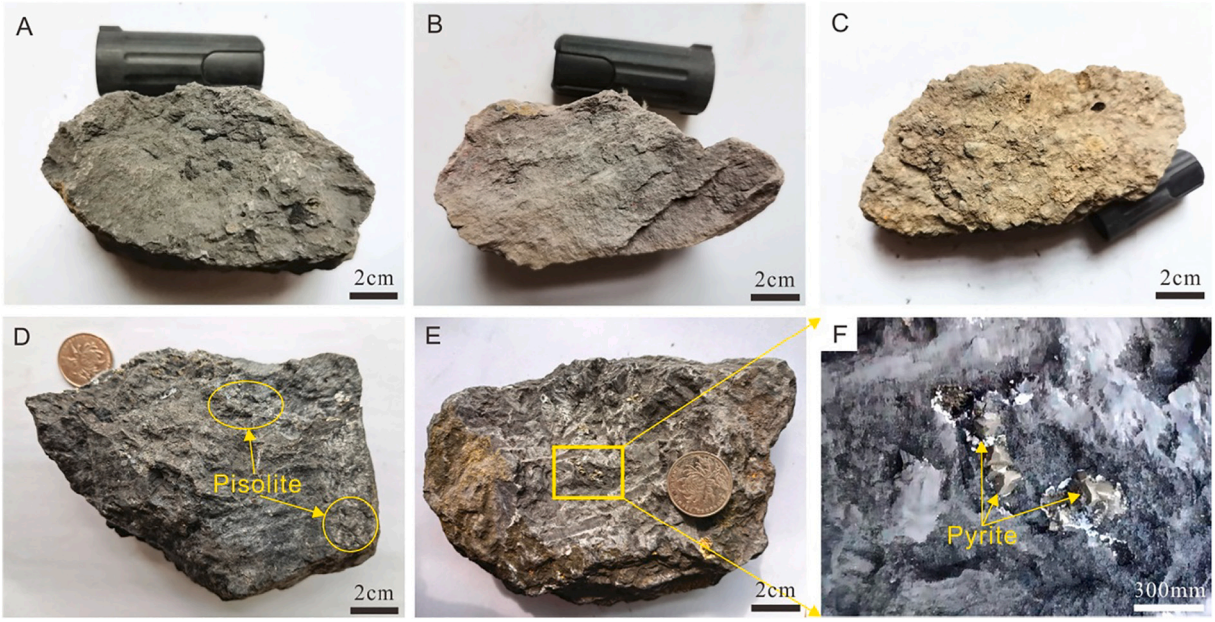

Fig. 2. Photographs of bauxite bed samples from the Pingguo area, western-central Guangxi region, SW China. (A–B) Clastic bauxite ores; (C) pisolitic bauxite ore; (D) claystone with pisolites; (E–F) claystone with authigenic pyrite.

et al., 2019; Bond et al., 2020), suggesting a causal link between the Emeishan LIP eruption and the Capitanian mass extinction. Coastal settings record stronger signals of terrestrial perturbations than shelf settings. However, Hg records in coastal settings during the Guadalupian–Lopingian biotic crisis remain uninvestigated, limiting our knowledge of the impact of the Emeishan LIP. We hereby investigated Hg contents and Hg isotope ratios, TOC contents and organic carbon isotope ratios, as well as element contents in proximal shelf shallow-water sections (bauxite beds) in the western-central Guangxi region, SW China, to constrain the intensity of the Emeishan LIP magmatism at the time of GLB and to evaluate its relationship to the Capitanian mass extinction.

2. Geological background

The GLB in the western-central Guangxi region, SW China, is recorded in the middle Permian Maokou Formation and the overlying upper Permian Heshan Formation. These strata are widely distributed in the Youjiang Basin, southwestern Yangtze Craton (Fig. 1). The Maokou Formation consists of thick bioclastic carbonates and calcarenites platform deposition, and cherts, cherty shale, and carbonate basinal deposits (Shen et al., 2007).

The global end-Guadalupian eustatic regression was one of the largest first-order lowstands in the Phanerozoic (Haq and Schutter, 2008). In southwest China, this regression was associated with the Dongwu orogeny (He et al., 2003; Sun et al., 2010). After that, massive volcanic eruptions occurred in the Emeishan LIP, which covered an area of >250,000 km^2 (Fig. 1A). The Emeishan LIP eruptions emitted massive amounts of greenhouse gases (e.g., CO_2), increasing global temperature and continental weathering (Wignall et al., 2009; Liu et al., 2017). Weathered materials were transported to the Youjiang Basin to form the Wuchiapingian clastic sedimentary rocks in the lowermost Xuanwei, Longtan, Wuchiaping, and Heshan formations (Fig. 1B).

The sedimentology and biostratigraphy constrain the maximum sea-level fall and subsequence onset of the GLB transgression to the end of *the Jinogondolella granti* zone (G7) in the Penglaitan section (Shen et al., 2007, 2019b; Wignall et al., 2009). During this period, the sea level fell in the western-central Guangxi region in the Youjiang Basin, which was temporally coincident with a depositional hiatus and bauxite beds formation (Shen et al., 2019b; Yu et al., 2019). This was terminated in the *Clarkina dukouensis* zone (L2) when a rapid rise in sea level occurred, reflected by deposition of Heshan Formation limestones upon the bauxite beds (Fig. 1B; Shen et al., 2007, 2019b).

Bauxite is a (paleo-) chemical residue of intense subaerial weathering formed under warm climatic conditions, with Al_2O_3 content >35% and an Al_2O_3/SiO_2 weight ratio > 2.6 (Bogatyrev et al., 2009). Bauxite deposits in the western-central Guangxi region were formed through the erosion of the Al_2O_3-rich residue that was transported to coastal settings and deposited in marine conditions (Yu et al., 2019). The bauxite beds in the Pingguo region are subdivided into a lower layer (0–8 m thick) of purple, grey, or black bauxite, and pisolitic and oolitic bauxite (Fig. 2A–C), and an overlying layer (0–10 m thick) of black carbonaceous claystones, with minor grey and white claystones and silty claystones (Fig. 2D–F; Deng et al., 2010; Liu et al., 2017).

Samples were collected from two sections at Xinxu (23°25′48″N, 107°35′20″E) and Jiaomei (23°35′13″N, 107°40′20″E) in the Pingguo area, western Guangxi, SW China (Fig. 1). The Xinxiu (XX) and Jiaomei (JM) sections both cover the whole unit of the lowermost Heshan Formation bauxite beds, which consist of the bauxites and overlying carbonaceous claystones.

3. Methods

The samples had weathered surfaces cut off, then were powdered to ~200 mesh in an agate mortar and pestle, and homogenised prior to chemical analysis. Representative samples were made into polished thin sections for scanning electron microscopy-energy dispersive spectrometry (SEM-EDS) observation and analysis using a Thermo Scientific Scios dual-beam SEM at the Institute of Geochemistry, Chinese Academy of Sciences (IGCAS).

3.1. Trace element analyses

Whole-rock trace element analyses were undertaken at IGCAS using a Plasma Quant-MS Elite inductively coupled plasma–mass spectrometer. Both procedural blanks and the national standards OU-6, AMH-1, and GBPG-1 were analysed for data quality control, which yielded an average recovery of 90% (n = 3) and reproducibility within less than ±10% for all trace elements.

3.2. Total Sulphur, total organic carbon, and organic carbon isotope analyses

Total sulphur (TS) and TOC analyses were conducted with an Elementar Vario Microcube analyzer at IGCAS, with analytical errors of less than ±2.5%. Prior to the analyses, the sample powders were leached with 2.5 N HCl to remove inorganic C. The residual powder was then rinsed with 18.2 MΩ·cm water and freeze-dried. For the organic stable C isotope analyses, the samples were first decarbonated with 2.5 N HCl for 12 h to remove inorganic C. After freeze-drying, the organic stable C isotopic compositions were measured with a MAT253 isotope ratio mass spectrometer, with an analytical uncertainty of ~0.2‰. The results (i.e., $\delta^{13}C_{org}$ values) are reported relative to the Vienna Pee Dee belemnite standard (V-PDB).

3.3. Mercury content and isotope analyses

Mercury contents were measured with a DMA-80 Hg analyzer at IGCAS, which yielded a Hg recovery of 90–110% (n = 4) and reproducibility within less than ±10% for SRM GSS-4. For the Hg isotope measurement, Hg in the samples was preconcentrated in 5 mL of 40% inverse aqua regia (HCl/HNO_3 = 1/3, v/v) using a dual-stage combustion furnace (Zerkle et al., 2020). The preconcentrated solutions were diluted to 1 ng/mL Hg and measured with a Neptune Plus multi-collector ICP-MS (Yin et al., 2016). Following the nomenclature by Blum and Bergquist (2007), MDF of Hg isotopes was expressed in the δ^{202}Hg notation in units of per mil (‰) relative to the NIST-3133 Hg standard (analysed before and after each sample):

$$\delta^{202}\mathrm{Hg}\ (‰) = \left[\left(^{202}\mathrm{Hg}/^{198}\mathrm{Hg}_{\mathrm{sample}}\right)/\left(^{202}\mathrm{Hg}/^{198}\mathrm{Hg}_{\mathrm{standard}}\right)-1\right] \times 1000 \quad (1)$$

MIF of Hg isotopes was reported in Δ notation:

$$\Delta^{199}\mathrm{Hg} \approx \delta^{199}\mathrm{Hg}–\delta^{202}\mathrm{Hg} \times 0.2520 \quad (2)$$

$$\Delta^{200}\mathrm{Hg} \approx \delta^{200}\mathrm{Hg}–\delta^{202}\mathrm{Hg} \times 0.5024 \quad (3)$$

$$\Delta^{201}\mathrm{Hg} \approx \delta^{201}\mathrm{Hg}–\delta^{202}\mathrm{Hg} \times 0.7520 \quad (4)$$

NIST-3177 standard solutions, diluted to 1 ng/mL Hg in 10% HCl, were measured in every 5–10 samples. The average and reproducibility of the data for NIST-3177 (δ^{202}Hg = −0.5‰ ± 0.1‰; Δ^{199}Hg = −0.01‰ ± 0.05‰; Δ^{201}Hg = −0.02‰ ± 0.07‰; 2SD; n = 11) and GSS-4 (δ^{202}Hg = −1.67‰ ± 0.14‰; Δ^{199}Hg = −0.34‰ ± 0.08‰; Δ^{201}Hg = −0.35‰ ± 0.07‰; 2SD; n = 3) agree well with previous studies (Blum and Bergquist, 2007; Yin et al., 2022). The larger of the two standard deviations (2SD) values obtained for NIST-3177 or GSS-4 are used to reflect the analytical uncertainties of the samples.

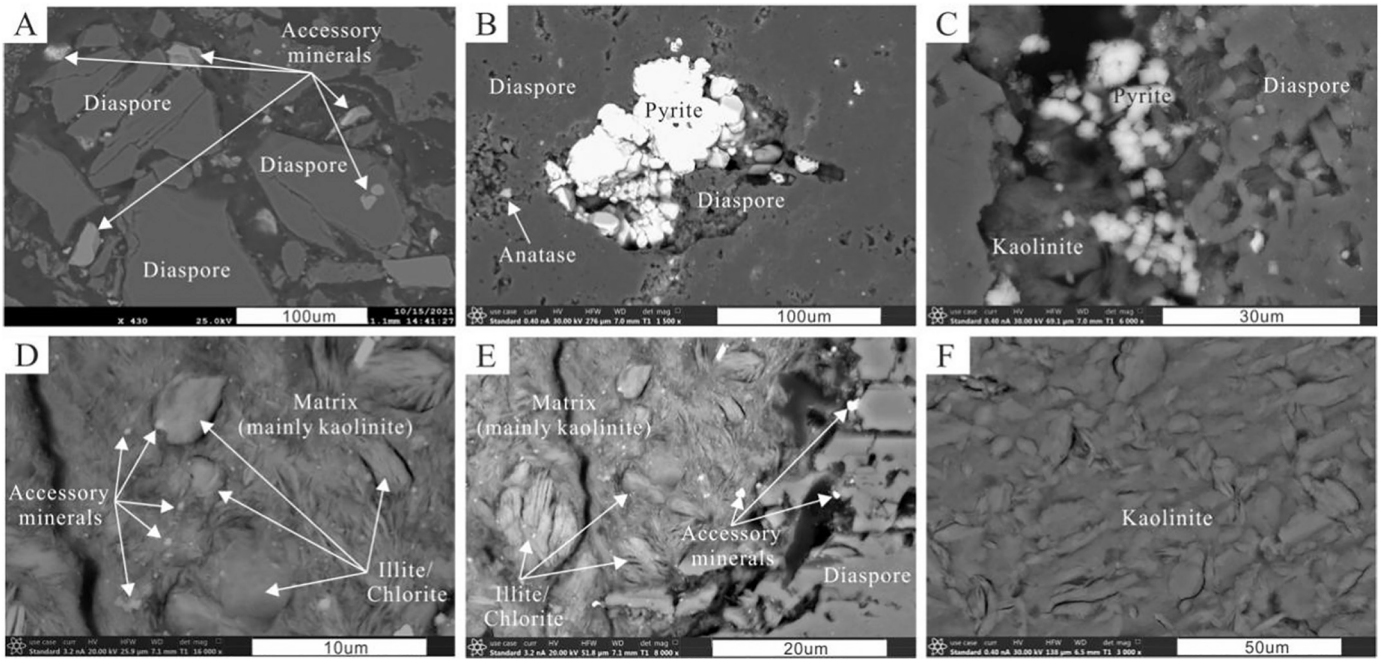

Fig. 3. Back-scattered electron (BSE) images of (A–C) bauxite and (D—F) claystone samples from the Pingguo area, western-central Guangxi region, SW China. (A) Coexisting coarse-grained (10–200 μm) platy diaspore and accessory minerals (mainly zircon and anatase with grain sizes 2–100 μm); (B) coexisting diaspore, anatase, and pyrite; (C) coexisting diaspore, pyrite, and kaolinite; (D-E) fine-grained (<2 μm) accessory and clay minerals (mainly illite and chlorite) distributed randomly in a kaolinite matrix; (F) kaolinite.

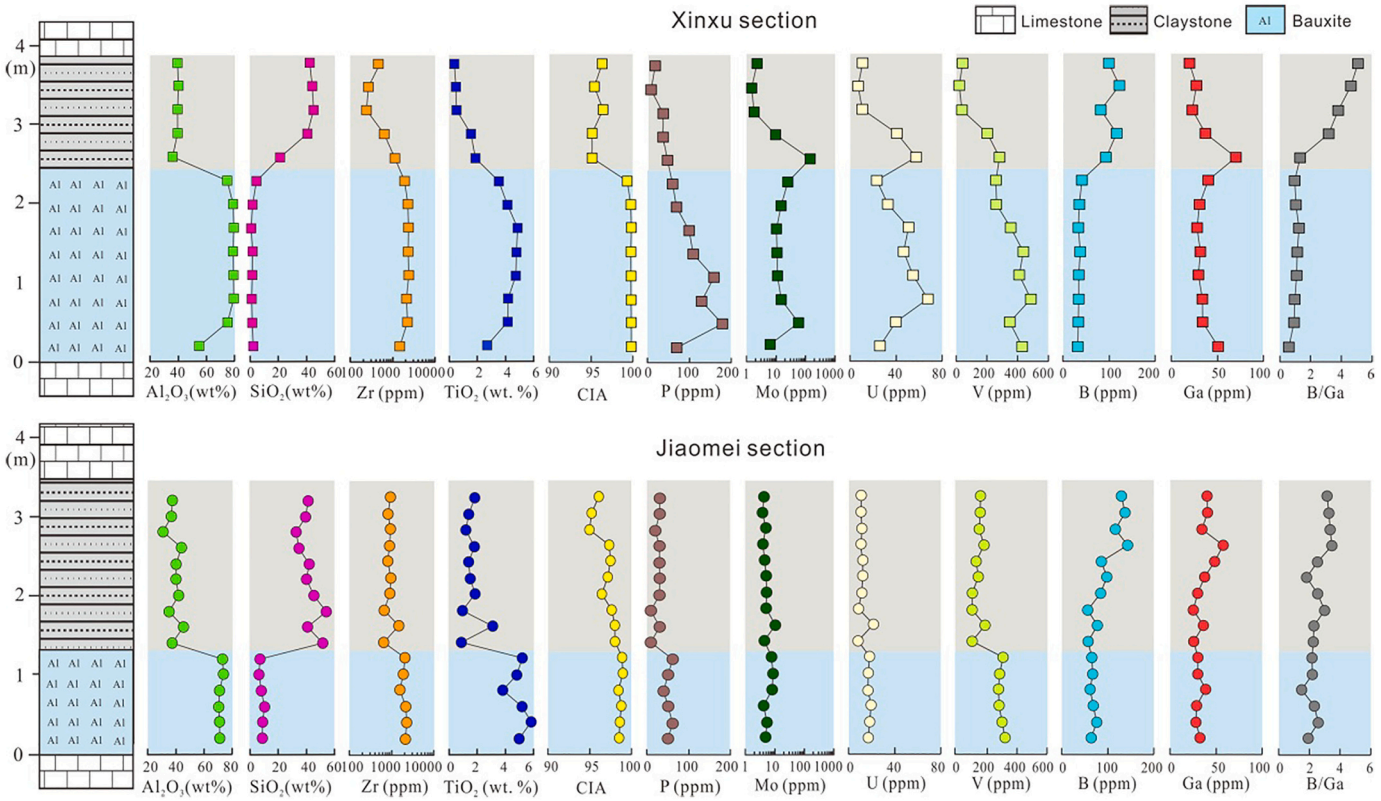

Fig. 4. Lithology, CIA values, and Al_2O_3, SiO_2, Zr, TiO_2, P, Mo, U, V, B, Ga, and clay contents of the Xinxu and Jiaomei sections, Pingguo area, western-central Guangxi region, SW China (Al_2O_3, SiO_2, TiO_2, Zr, and clay contents and CIA values from Ling et al., 2021).

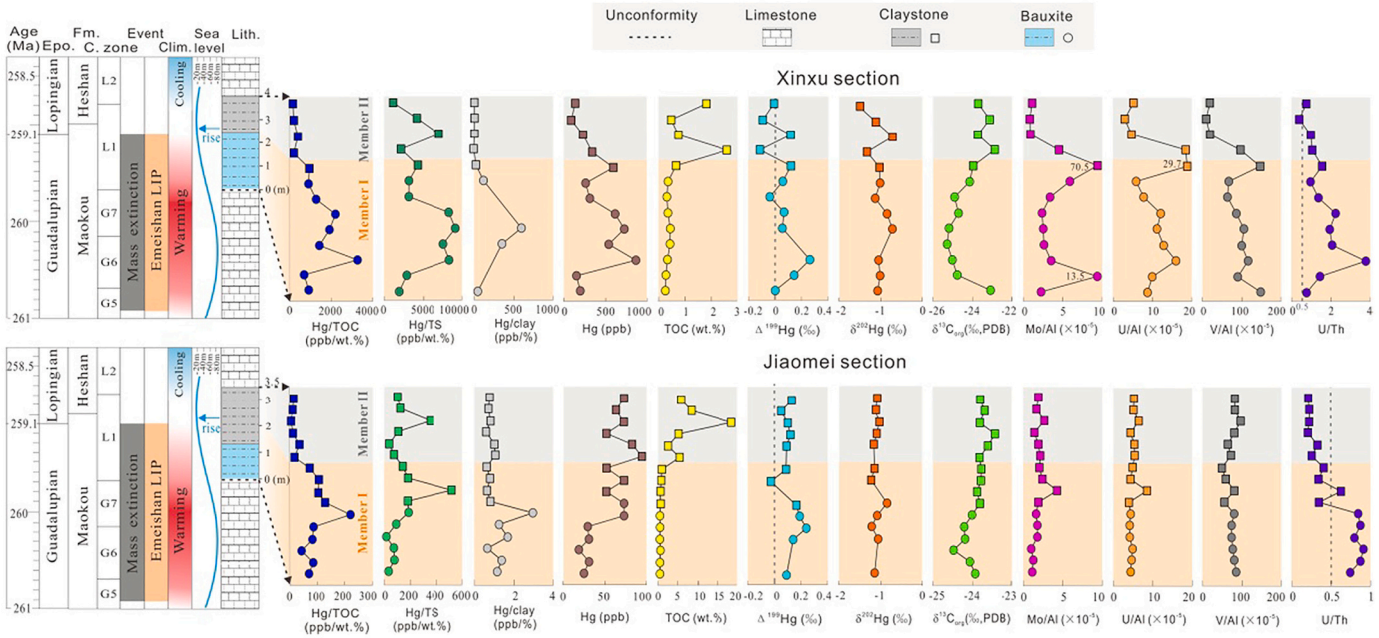

Fig. 5. Lithology and TOC contents, Hg contents, Hg/TOC ratios, Hg/TS ratios, Hg/clay ratios, stable Hg isotopic compositions, organic stable C isotopic compositions, B/Ga ratios, and oceanic redox conditions (Mo/Al, U/Al, V/Al, and U/Th ratios) of the Xinxu and Jiaomei sections, Pingguo area, western-central Guangxi region, SW China. Also shown are conodont zones (Yuan et al., 2019), mass extinction events (Zhang et al., 2015; Bond et al., 2010), age of the Emeishan LIP (Zhong et al., 2014), climatic changes (Wang et al., 2020), and sea-level changes (Haq and Schutter, 2008). Epo. = epoch; Fm. = formation; C. zone = conodont zone; Clim. = climate; Lith. = lithology; G5 = *Jinogondolella prexuanhanensis* zone; G6 = *Jinogondolella xuanhanensis* zone; G7 = *Jinogondolella granti* zone; L1 = *Clarkina postbitteri hongshuiensis* to *Clarkina postbitteri postbitteri* zones; L2 = *Clarkina dukouensis* zone. Both sections were divided into Member I (i.e., the peak stage of Emeishan LIP volcanism) and Member II (i.e., the waning stage of Emeishan LIP volcanism) based on Hg/TOC ratios.

4. Results

4.1. Mineralogy

SEM-EDS analyses showed that the Heshan formation bauxite ores consist of diaspore and small amounts of clay minerals (illite, kaolinite, and chlorite), accessory minerals (anatase and zircon) and Fe-rich minerals (pyrite and goethite) (Figs. 3A–C). The diaspore has short prismatic or platy shapes and is typically 10–100 μm in size. The accessory minerals are 2 to >100 μm in size, and some occur as automorphic or hypautomorphic grains. Pyrite often occurs in aggregates with a mineral size of <5 μm, indicative of a sedimentary origin. The overlying claystones (mudstones) contain a variety of minerals, including chlorite, illite, kaolinite, diaspore, anatase, zircon, and pyrite (Figs. 3D–F). The pyrite occurs commonly as automorphic grains with variable sizes (50–200 μm) and is easy to identify in hand specimens. Most of the clay minerals are small (<2 μm) and typically coexist, and have hair-like or, more rarely, platy morphologies (>10 μm). In contrast, the accessory minerals are typically small (<2 μm) and generally randomly distributed in the samples. The accessory minerals in bauxites have larger grain sizes than those in claystones (Fig. 3), suggesting that bauxites were formed at shallower depths than the claystones.

4.2. Elemental geochemistry

The two sections show similar major element concentrations (Table S1; Fig. 4). The bauxites have high Al_2O_3 and TiO_2 contents, and comparatively low SiO_2 contents (Table S1; Fig. 4). The claystones have lower Al_2O_3 and TiO_2, and higher SiO_2 contents than the bauxites (Table S1). High chemical index of alteration (CIA) values of bauxite ores (98.5–99.9) and claystones (92.8–98.1) are consistent with strong chemical weathering (Table S1). The Jiaomei section has higher total sulphur (TS) contents (0.1–2.4 wt%) than the Xinxu section (0.02–0.16 wt%) (Table S2).

The two sections show large differences in trace elements concentrations (Table S1; Fig. 4). The Xinxu section has higher contents of Mo, U, Th, V, and P but lower contents of B and Ga than the Jiaomei section. However, they have similar trends, in that Mo, U, V, Zr, Ti, and P decrease and B and Ga increase gradually upward except for the lowermost samples in the Xinxu section (Table S1; Fig. 4). Redox-sensitive elements Mo, U, and V are a reliable proxy of redox conditions in the depositional/diagenetic environment (e.g., Tribovillard et al., 2006). In the Xinxu section, Member I has higher Mo/Al, U/Al, V/Al, and U/Th ratios than Member II (Fig. 5). The B/Ga ratios, indicative of seawater salinity (Wei and Algeo, 2020), gradually increase upsection in both sections, consistent with the transgression process during that time (Fig. 4). Furthermore, the relatively lower B/Ga ratios in the Xinxu section (average 2) indicates that it was deposited in a shallower water depth than the Jiaomei section (average 2.5) (Table S1).

4.3. Total organic carbon contents and stable carbon isotopic compositions

The TOC contents of Member I are low (<0.8 wt.‰) in both the Xinxu and Jiaomei sections, but increase abruptly up to 2.56 and 18.4 wt%, respectively, in Member II. Similar $\delta^{13}C_{org}$ trends characterise both sections, with a notable negative excursion (up to ~2.5‰) in Member I (Table S2; Fig. 5).

4.4. Mercury contents, Hg/TOC ratios and Hg isotope composition

In the Xinxu section, Hg contents decrease from the peak values (167–865 ppb) in Member I to 83–344 ppb in Member II. In the Jiaomei section, Hg contents increase gradually from 19 to 73 ppb in Member I to 52–94 ppb in Member II. Notably high Hg/TOC ratios can be observed near the GLB in both sections, with peak Hg/TOC ratios of 3330 and 221 ppb/wt%, respectively, which are remarkably higher than global marine sediments (~71.9 ppb/wt%, Grasby et al., 2019).

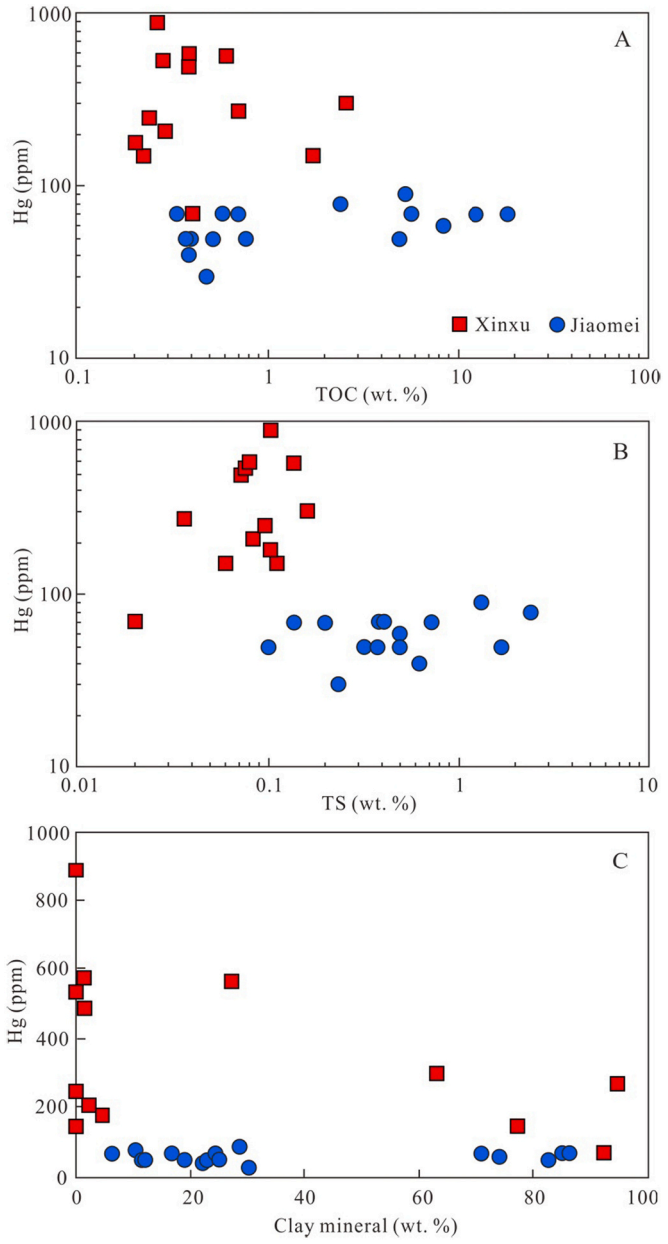

Fig. 6. Plots of Hg contents versus (A) TOC, (B) TS, and (C) clay mineral contents in the Xinxu and Jiaomei sections. Data for the clay mineral compositions are from Ling et al. (2021).

δ^{202}Hg and Δ^{199}Hg values vary from −1.54‰ to −0.72‰ and −0.11‰ to 0.26‰ in the two sections (Table S2 and Fig. 5). δ^{202}Hg values fluctuate around a value of −1.0‰ and show no clear patterns. Both sections have negative shifts of Δ^{199}Hg from Member I to Member II.

5. Discussion

5.1. Causal links between Hg anomalies and the Emeishan large igneous province

The main host phases of Hg in sediments are organic matter, sulphides, and clay minerals (Grasby et al., 2019; Shen et al., 2020). In the two studied sections, no significant correlations can be found between Hg and TOC ($p < 0.05$), Hg and TS ($p < 0.05$), and Hg and clay contents ($p < 0.05$), suggesting that Hg exists in multiple phases in the samples (Fig. 6). The anomalous high Hg/TOC, Hg/TS and Hg/clay ratios in the bauxite bed samples suggest enhanced Hg inputs into the ocean, rather than drawdown of organic matter, sulphides and clay materials (Fig. 5). Marine sediments show average Hg/TOC ratios of ~71.9 ppb/wt% (Grasby et al., 2019). In this study, the anomalous high Hg/TOC ratios (up to 3330 and 221 ppb/wt%, respectively) in the Xinxu and Jiaomei sections are consistent with excess Hg loading, potentially from volcanism, during the formation of bauxite beds. Similar Hg anomalies have also been observed around the GLB in distal shelf and slop/basinal depositional settings, which have been interpreted to be a result of the Emeishan LIP (Grasby et al., 2016; Huang et al., 2019; Bond et al., 2020).

The main stage of the Emeishan LIP occurred between ca. 260.9 and 259.1 Ma, and its waning stage may have continued until ca. 257.4 Ma (Zhong et al., 2014). Detrital zircon studies of bauxites from the Pingguo area have revealed a dominant age peak at 261 ± 2 Ma, corresponding to the age of the Emeishan LIP (Deng et al., 2010). In our study, the coincidence of Hg anomalies in the bauxite bed and the Emeishan LIP further supports their causal link (Fig. 5). The correlated increases in Hg contents, Hg/TOC ratios, and Δ^{199}Hg values in the lowermost part of both sections (Member I) appear to represent the peak stage of the Emeishan LIP (Fig. 5). The near zero to positive Δ^{199}Hg (−0.04‰ to +0.26‰) values in the bauxite beds support extensive volcanic Hg deposition as a cause of the Hg anomalies, mainly via wet Hg(II) deposition (Zhou et al., 2021; Grasby et al., 2019). Intense Emeishan LIP magmatism at the end-Guadalupian would have released a large amount of Hg into the atmosphere, which we interpret to be responsible for the significant Hg/TOC anomalies in Member I in the two studied sections.

The Hg/TOC ratios remain high in Member I in the two studied sections, until the *Clarkina postbitteri postbitteri* zone (L1), the base of which marks the end of the peak stage of Emeishan LIP volcanism at ca. 259.1 Ma (Zhong et al., 2014). This implies that constant intense eruptions during the peak stage of the Emeishan LIP at the end-Guadalupian may have caused the large Hg anomalies in Member I. In contrast, the moderate Hg anomalies in Member II may be explained by a decreasing volcanic input into the atmosphere during the waning stages of the Emeishan LIP in the earliest Lopingian. The gradual decrease in Δ^{199}Hg values up-section supports this hypothesis (Fig. 5).

5.2. Link between the Emeishan large igneous province and the Capitanian mass extinction

The occurrence of autogenetic pyrite (Figs. 3B and C) and higher U/Th, Mo/Al, U/Al, and V/Al ratios in Member I (mainly bauxites) suggest anoxic conditions, given that sediments with U/Th ratios of >0.5 and < 0.5 reflect anoxic and oxic conditons, respectively (Fig. 5; Wignall and Twitchett, 1996). Intense volcanism related to the emplacement of LIPs is considered to be an important trigger of OAEs and related major environmental changes (Bond and Grasby, 2017). The immediate aftermath of LIP activity results in a sustained release of volcanic CO_2 (Naafs et al., 2016), which triggers rapid global warming and elevated silicate weathering rates. This increases the nutrient (e.g., P, N, and Fe) supply to the ocean and enhances biological productivity, reduces oxygen solubility, and increases ocean stratification, which could be an important cause of expanded oceanic anoxia (Tejada et al., 2009; Zhang et al., 2018). Based on the enhanced silicate weathering (as suggested by high CIA values and Zr and TiO_2 contents), elevated nutrient input (as indicated by high P contents) to the ocean, and anoxic depositional condition recorded by the bauxites in both sections, we suggest that the Emeishan LIP volcanism led to an expansion of marine anoxia and bauxite formation, which is consistent with mineralogical study conducted by Liu et al. (2017). The negative $\delta^{13}C_{org}$ excursion (~2.5‰) in Member I in both sections suggests that the Emeishan LIP eruptions had a profound impact on the C cycle during this time, likely due to the release of massive amounts of ^{13}C-depleted CO_2 and CH_4 by magmatic degassing and contact metamorphic degassing around sub-volcanic intrusions (Fig. 5; Svensen et al., 2004; Self et al., 2005; Percival et al.,

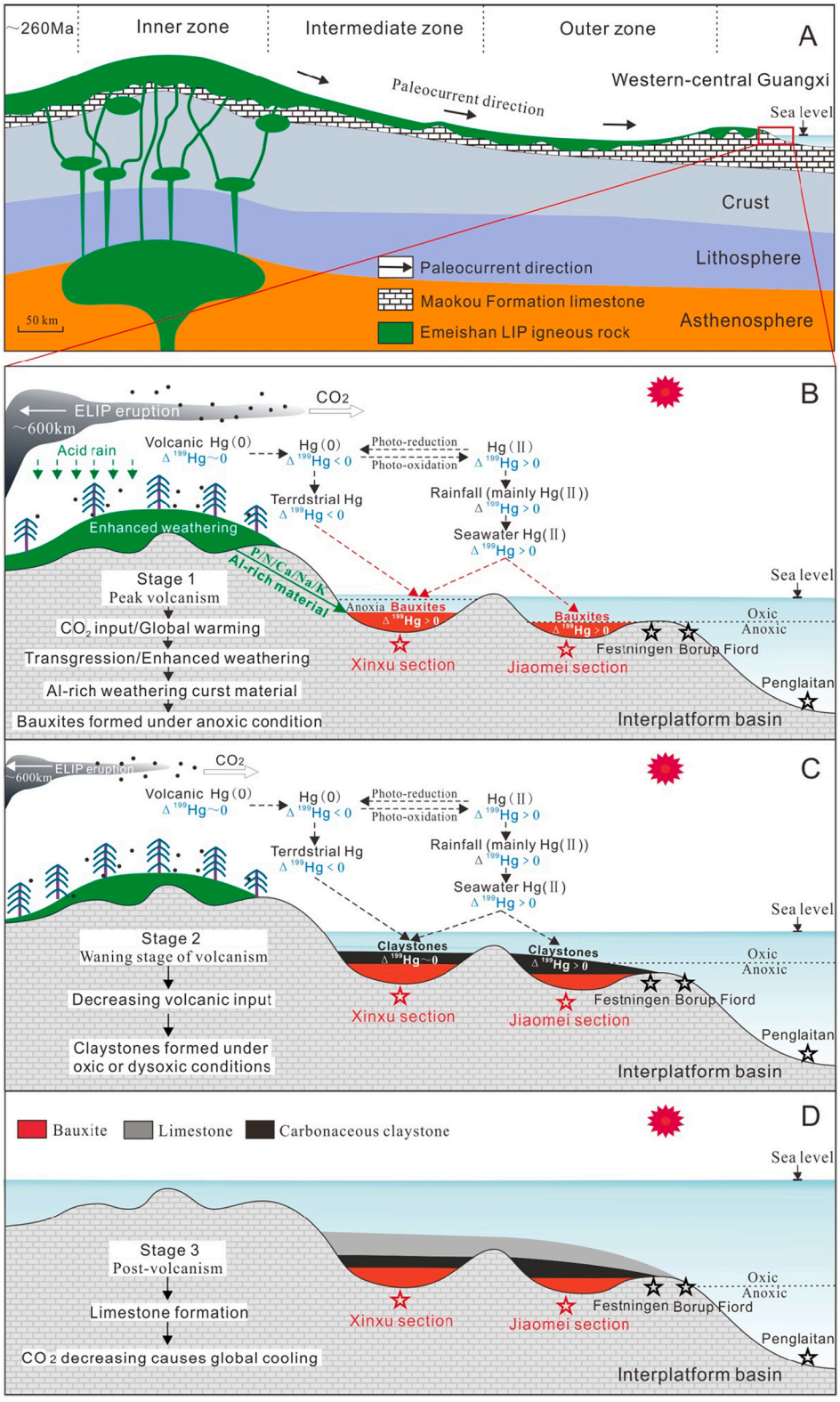

Fig. 7. Model of the development of the GLB in the western-central Guangxi region, SW China. The geodynamic setting of the Emeishan LIP is modified from Liu et al. (2017). The model highlights the mechanisms of MIF of Hg in the bauxite bed in the Pingguo area, western-central Guangxi region. Red stars represent the sampling points of this study and black stars represent the location of the Festningen section, Spitsbergen, Norway, Borup Fiord section, Arctic Canada, and the Penglantan section, central Guguangxi region, SW China (Grasby et al., 2016; Huang et al., 2019; Bond et al., 2020). (For interpretation of the references to colour in this figure legend, the reader is referred to the web version of this article.)

2018; Jones et al., 2016, 2019). In contrast, the claystones that formed under oxic or weakly reducing conditions have lower CIA values and P, Zr, and TiO_2 contents, which can be explained by the waning of the Emeishan LIP.

Fossil data for the global stratotype section and point (GSSP) in the Penglaitan and Tieqiao sections indicate that the protracted Capitanian mass extinction lasted from the *Jinogondolella xuanhanensis* zone (G6) to the GLB (Mei et al., 1998; Jin et al., 2006; Zhang et al., 2015). In the present study, the peak stage of Emeishan LIP volcanism coincided with a negative $\delta^{13}C_{org}$ excursion (Fig. 5), Hg/TOC anomalies, mass extinction, widespread marine anoxia, and sea-level rise. The temporal link between these phenomena suggests that marine anoxia caused by the Emeishan LIP was a contributor to the Capitanian mass extinction.

Our results offer insights into the climate/ocean dynamics, global

ecosystems and the formation of bauxite beds during the GLB, as follows:

Stage 1 (Fig. 7A–B): At the middle Permian (early- and middle-Capitanian), the eruption of Emeishan LIP released atmospheric Hg and greenhouse gases (e.g., CO_2), supported by high Hg/TOC anomalies and positive Δ^{199}Hg values in Member I (end-Capitanian), resulting in global warming, enhanced silicate weathering, and marine anoxia to spread to shelf regions, which favored bauxite deposition and could play a critical role in causing the Capitanian mass extinction, as evidenced by the negative $\delta^{13}C_{org}$ excursion in Member I.

Stage 2 (Fig. 7C): At the beginning of the Lopingian, the Emeishan LIP volcanism waned, which led to a slight decrease in the rate of silicate weathering and nutrient input into the ocean, and eventually caused the reduction of anoxic waters, in which the claystones were deposited under oxic or dysoxic conditions. During this stage, the amount of Hg deposited in the Member II decreased significantly in the Xinxu section due to a reduction in the external Hg supply, as evidenced by the decrease in Hg/TOC ratios and Δ^{199}Hg values in both the Xinxu and Jiaomei sections.

Stage 3 (Fig. 7D): During the early Lopingian (i.e., the *Clarkina dukouensis* zone), a rapid rise in sea level formed the Heshan Formation limestones, which overlie the bauxite bed (Shen et al., 2007, 2019b).

6. Conclusions and implications

This study observes anomalous high Hg concentrations and positive Δ^{199}Hg values in bauxite beds formed at the GLB in the western Guangxi region, China, which suggest extensive volcanic Hg input (from the Emeishan LIP eruption) to the ocean via wet Hg(II) deposition. LIP eruption could have released large amounts of CO_2 into the atmosphere, resulting in global warming, the formation of the bauxite bed. The peak stage of Emeishan LIP volcanism coincided with a negative $\delta^{13}C_{org}$ excursion, Hg/TOC anomalies, mass extinction, widespread marine anoxia, and sea-level rise, suggesting the Emeishan LIP as a driving force for the climate/ocean dynamics and global ecosystems during the GLB, although ocean acidification is thought to be the direct cause of biological stress (Sanei et al., 2012; Bond et al., 2010, 2015, 2020).

Declaration of Competing Interest

The authors declare that they have no known competing financial interests or personal relationships that could have appeared to influence the work reported in this paper.

Data availability

Data will be made available on request.

Acknowledgements

This work was supported by the National Key R&D Program of China (grant 2022YFC2903402), the National Natural Science Foundation of China (grants 92062107, 92162214), the Key R&D Program of Yunan Province (graint 202103AQ100003), the Key Research Program of the Chinese Academy of Sciences (grant ZDRW-ZS-2020-4-1), and the Key Research Program of the Institute of Geology & Geophysics, CAS (Grant IGGCAS-201902).

Appendix A. Supplementary data

Supplementary data to this article can be found online at https://doi.org/10.1016/j.chemgeo.2022.121243.

References

Blum, J.D., Bergquist, B.A., 2007. Reporting the variations in the natural isotopic composition of mercury. Anal. Bioanal. Chem. 388, 353–359.
Blum, J.D., Sherman, L.S., Johnson, M.W., 2014. Mercury Isotopes in Earth and Environmental Sciences. Annu. Rev. Earth Planet. Sci. 42, 249–269.
Bogatyrev, B.A., Zhukov, V.V., Tsekhovsky, Y.G., 2009. Phanerozoic bauxite epochs. Geol. Ore Dep. 51 (6), 456–466.
Bond, D.P.G., Grasby, S.E., 2017. On the causes of mass extinctions. Palaeogeogr. Palaeoclimatol. Palaeoecol. 478, 3–29.
Bond, D.P.G., Hilton, J., Wignall, P.B., Ali, J.R., Stevens, L.G., Sun, Y.-D., Lai, X.-L., 2010. The Middle Permian (Capitanian) mass extinction on land and in the oceans. Earth-Sci. Rev. 102, 100–116.
Bond, D.P.G., Wignall, P.B., Joachimski, M.M., Sun, Y.D., Savov, I., Grasby, S.E., Beauchamp, B., Blomeier, D.P.G., 2015. An abrupt extinction in the Middle Permian (Capitanian) of the Boreal Realm (Spitsbergen) and its link to anoxia and acidification. Geol. Soc. Am. Bull. 127, 1411–1421.
Bond, D.P.G., Wignall, P.B., Grasby, S.E., 2020. The Capitanian (Guadalupian, Middle Permian) mass extinction in NW Pangea (Borup Fiord, Arctic Canada): a global crisis driven by volcanism and anoxia. Geol. Soc. Am. Bull. 132, 931–942.
Deng, J., Wang, Q.F., Yang, S.J., Liu, X.F., Zhang, Q.Z., Yang, L.Q., Yang, Y.H., 2010. Genetic relationship between the Emeishan plume and the bauxite deposits in western Guangxi, China: constraints from U–Pb and Lu–Hf isotopes of the detrital zircons in bauxite ores. J. Asian Earth Sci. 37, 412–424.
Gong, Q., Wang, X., Zhao, L., Grasby, S.E., Chen, Z.-Q., Zhang, L., Li, Y., Cao, L., Li, Z., 2017. Mercury spikes suggest volcanic driver of the Ordovician-Silurian mass extinction. Sci. Rep. 7 (1), 5304.
Grasby, S.E., Beauchamp, B., Bond, D.P.G., Wignall, P.B., Sanei, H., 2016. Mercury anomalies associated with three extinction events (Capitanian crisis, latest Permian extinction and the Smithian/Spathian extinction) in NW Pangea. Geol. Mag. 153, 285–297.
Grasby, S.E., Shen, W., Yin, R., Gleason, J.D., Blum, J.D., Lepak, R.F., Hurley, J.P., Beauchamp, B., 2017. Isotopic signatures of mercury contamination in latest Permian oceans. Geology 45, 55–58.
Grasby, S.E., Them, T.R., Chen, Z.H., Yin, R.S., Ardakani, O.H., 2019. Mercury as a proxy for volcanic emissions in the geologic record. Earth-Sci. Rev. 196, 102880.
Grasby, S.E., Liu, X., Yin, R., Ernst, R.E., Chen, Z., 2020. Toxic mercury pulses into late Permian terrestrial and marine environments. Geology 48 (8), 830–833.
Grasby, S.E., Bond, D.P.G., Wignall, P.B., Yin, R., Strachan, L.J., Takahashi, S., 2021. Transient Permian-Triassic euxinia in the southern Panthalassa deep ocean. Geology 49 (8), 889–893.
Haq, B.U., Schutter, S.R., 2008. A chronology of paleozoic sea-level changes. Science 322, 64–68.
He, B., Xu, Y.-G., Chung, S.-L., Xiao, L., Wang, Y., 2003. Sedimentary evidence for a rapid, kilometer-scale crustal doming prior to the eruption of the Emeishan flood basalts. Earth Planet. Sci. Lett. 213, 391–405.
Huang, Y., Chen, Z., Wignall, P.B., Grasby, S.E., Zhao, L., Wang, X., Kaiho, K., 2019. Biotic responses to volatile volcanism and environmental stresses over the Guadalupian-Lopingian (Permian) transition. Geology 47, 175–178.
Isozaki, Y., 2007. Plume Winter Scenario for Biosphere Catastrophe: the Permo-Triassic boundary Case, Superplumes: Beyond Plate Tectonics. Springer, pp. 409–440.
Jin, Y.G., Shen, S.Z., Henderson, C.M., Wang, X.D., Wang, W., Wang, Y., Cao, C.Q., Shang, Q.H., 2006. The Global Stratotype Section and Point (GSSP) for the boundary between the Capitanian and Wuchiapingian Stage (Permian). Episodes 29, 253–262.
Jones, M.T., Jerram, D.A., Svensen, H.H., Grove, C., 2016. The effects of large igneous provinces on the global carbon and Sulphur cycles. Palaeogeogr. Palaeoclimatol. Palaeoecol. 441, 4–21.
Jones, M.T., Percival, L.M., Stokke, E.W., Frieling, J., Mather, T.A., Riber, L., Schubert, B. A., Schultz, B., Tegner, C., Planke, S., Svensen, H.H., 2019. Mercury anomalies across the Palaeocene–Eocene thermal maximum. Clim. Past 15 (1), 217–236.
Ling, K.Y., Wen, H.J., Zhang, Q.Z., Luo, C.G., Gu, H.N., Du, S.J., Yu, X.W., 2021. Super-enrichment of lithium and niobium in the Upper Permian Heshan Formation in Pingguo, Guangxi, China. Sci. China Earth Sci. 64, 753–772.
Liu, X., Wang, Q., Zhang, Q., Yang, S., Liang, Y., Zhang, Y., Li, Y., Guan, T., 2017. Genesis of the Permian karstic Pingguo bauxite deposit, western Guangxi, China. Mineral. Deposita 52, 1031–1048.
McGhee, G.R., Clapham, M.E., Sheehan, P.M., Bottjer, D.J., Droser, M.L., 2013. A new ecological-severity ranking of major Phanerozoic biodiversity crises. Palaeogeogr. Palaeoclimatol. Palaeoecol. 370, 260–270.
Mei, S., Jin, Y., Wardlow, B.R., 1998. Conodont succession of the Guadalupian-Lopingian boundary strata in Laibin of Guangxi, China and West Texas, USA. Palaeoworld 9, 53–76.
Moynier, F., Jackson, M.G., Zhang, K., Cai, H., Halldórsson, S.A., Pik, R., Day, J.M.D., Chen, J., 2021. The mercury isotopic composition of earth's mantle and the use of mass independently fractionated Hg to test for recycled crust. Geophys. Res. Lett. 48 (17) e2021GL094301.
Naafs, B.D., Castro, J.M., De Gea, G.A., Quijano, M.L., Schmidt, D.N., Pancost, R.D., 2016. Gradual and sustained carbon dioxide release during Aptian Oceanic Anoxic Event 1a. Nat. Geosci. 9, 135–139.
Percival, L.M., Jenkyns, H.C., Mather, T.A., Dickson, A.J., Batenburg, S.J., Ruhl, M., Hesselbo, S.P., Barclay, R., Jarvis, I., Robinson, S.A., Woelders, L., 2018. Does large igneous province volcanism always perturb the mercury cycle? Comparing the records of Oceanic Anoxic Event 2 and the end-Cretaceous to other Mesozoic events. Am. J. Sci. 318 (8), 799–860.
Retallack, G.J., Metzger, C.A., Greaver, T., Jahren, A.H., Smith, R.M.H., Sheldon, N.D., 2006. Middle–Late Permian mass extinction on land. Geol. Soc. Am. Bull. 118, 1398–1411.
Sanei, H., Grasby, S.E., Beauchamp, B., 2012. Latest Permian mercury anomalies. Geology 40, 63–66.

Self, S., Thordarson, T., Widdowson, M., 2005. Gas fluxes from flood basalt eruptions. Elements 1, 283–287.
Shen, S.Z., Wang, Y., Henderson, C.M., Cao, C.Q., Wang, W., 2007. Biostratigraphy and lithofacies of the Permian System in the Laibin–Heshan area of Guangxi, South China. Palaeoworld 16, 120–139.
Shen, J., Chen, J., Algeo, T.J., Yuan, S., Feng, Q., Yu, J., Zhou, L., O'Connell, B., Planavsky, N.J., 2019a. Evidence for a prolonged Permian–Triassic extinction interval from global marine mercury records. Nat. Commun. 10 (1), 1–9.
Shen, S.Z., Zhang, H., Zhang, Y.C., Yuan, D.X., Chen, B., He, W.H., Mu, L., Lin, W., Wang, W.Q., Chen, J., Wu, Q., Cao, C.Q., Wang, Y., Wang, X.D., 2019b. Permian integrative stratigraphy and timescale of China. Sci. China Earth Sci. 62, 154–188.
Shen, J., Chen, J., Algeo, T.J., Feng, Q., Yu, J., Xu, Y.G., Xu, G., Lei, Y., Planavsky, N.J., Xie, S., 2020. Mercury fluxes record regional volcanism in the South China craton prior to the end-Permian mass extinction. Geology 49, 452–456.
Shen, J., Yin, R., Algeo, T.J., Svensen, H.H., Schoepfer, S.D., 2022. Mercury evidence for combustion of organic-rich sediments during the end-Triassic crisis. Nat. Commun. 13, 1307.
Stevens, L.G., Hilton, J., Bond, D.P.G., Glasspool, I.J., Jardine, P.E., 2011. Radiation and extinction patterns in Permian floras from North China as indicators for environmental and climate change. J. Geol. Soc. Lond. 168, 607–619.
Sun, Y., Lai, X.L., Wignall, P.B., Widdowson, M., Ali, J.R., Jiang, H.S., Wang, W., Yan, C. B., Bond, D.P.G., Védrine, S., 2010. Dating the onset and nature of the Middle Permian Emeishan large igneous province eruptions in SW China using conodont biostratigraphy and its bearing on mantle plume uplift models. Lithos 119, 20–33.
Svensen, H., Planke, S., Malthe-Sørenssen, A., Jamtveit, B., Myklebust, R., Rasmussen Eidem, T., Rey, S.S., 2004. Release of methane from a volcanic basin as a mechanism for initial Eocene global warming. Nature 429, 542–545.
Tejada, M.L.G., Suzuki, K., Kuroda, J., Coccioni, R., Mahoney, J.J., Ohkouchi, N., Sakamoto, T., Tatsumi, Y., 2009. Ontong Java Plateau eruption as a trigger for the early Aptian oceanic anoxic event. Geology 37, 855–858.
Thibodeau, A.M., Ritterbush, K., Yager, J.A., West, A.J., Ibarra, Y., Bottjer, D.J., Berelson, W.M., Bergquist, B.A., Corsetti, F.A., 2016. Mercury anomalies and the timing of biotic recovery following the end–Triassic mass extinction. Nat. Commun. 7, 11147.
Tribovillard, N., Algeo, T.J., Lyons, T., Riboulleau, A., 2006. Trace metals as paleoredox and paleoproductivity proxies: an update. Chem. Geol. 232 (1), 12–32.
Wang, W., Garbelli, C., Zhang, F., Zheng, Q., Zhang, Y., Yuan, D., Shi, Y., Chen, B., Shen, S., 2020. A high-resolution Middle to Late Permian paleotemperature curve reconstructed using oxygen isotopes of well-preserved brachiopod shells. Earth Planet. Sci. Lett. 540, 116245.
Wang, X., Cawood, P.A., Grasby, S.E., Zhao, L., Chen, Z., Wu, S., Huang, Y., 2021. Characteristics of Hg concentrations and isotopes in terrestrial and marine facies across the end-Permian mass extinction. Glob. Planet. Chang. 205, 103592.
Wei, W., Algeo, T.J., 2020. Elemental proxies for paleosalinity analysis of ancient shales and mudrocks. Geochim. Cosmochim. Acta 287, 341–366.
Wignall, P.B., Twitchett, R.J., 1996. Oceanic anoxia and the end-Permian mass extinction. Science 272, 1155–1158.
Wignall, P.B., Sun, Y.D., Bond, D.P., Izon, G., Newton, R.J., Védrine, S., Widdowson, M., Ali, J.R., Lai, X.L., Jiang, H.S., Cope, H., Bottrell, S.H., 2009. Volcanism, mass extinction, and carbon isotope fluctuations in the Middle Permian of China. Science 324, 1179–1182.
Yin, R., Krabbenhoft, D.P., Bergquist, B.A., Zheng, W., Lepak, R.F., Hurley, J.P., 2016. Effects of mercury and thallium concentrations on high precision determination of mercury isotopic composition by Neptune Plus multiple collector inductively coupled plasma mass spectrometry. J. Anal. Atom. Spectrom. 31 (10), 2060–2068.
Yin, R., Chen, D., Pan, X., Deng, C., Chen, L., Song, X., Yu, S., Zhu, C., Wei, X., Xu, Y., Feng, X., Blum, J.D., Lehmann, B., 2022. Mantle Hg isotopic heterogeneity and evidence of oceanic Hg recycling into the mantle. Nat. Commun. 13, 948.
Yu, W., Algeo, T.J., Yan, J., Yang, J., Du, Y., Huang, X., Weng, S., 2019. Climatic and hydrologic controls on upper Paleozoic bauxite deposits in South China. Earth-Sci. Rev. 189, 159–176.
Yuan, D.X., Shen, S.Z., Henderson, C.M., Chen, J., Zhang, H., Zheng, Q.F., Wu, H., 2019. Integrative timescale for the Lopingian (Late Permian): a review and update from Shangsi, South China. Earth-Sci. Rev. 188, 190–209.
Zambardi, T., Sonke, J.E., Toutain, J.P., Sortino, F., Shinohara, H., 2009. Mercury emissions and stable isotopic compositions at Vulcano Island (Italy). Earth Planet. Sci. Lett. 277, 236–243.
Zerkle, A.L., Yin, R., Chen, C., Li, X., Izon, G.J., Grasby, S.E., 2020. Anomalous fractionation of mercury isotopes in the Late Archean atmosphere. Nat. Commun. 11, 1–9.
Zhang, G., Zhang, X., Li, D., Farquhar, J., Shen, S., Chen, X., Shen, Y., 2015. Widespread shoaling of sulfidic waters linked to the end-Guadalupian (Permian) mass extinction. Geology 43, 1091–1094.
Zhang, F., Romaniello, S.J., Algeo, T.J., Lau, K.V., Clapham, M.E., Richoz, S., Herrmann, A.D., Smith, H., Horacek, M., Anbar, A.D., 2018. Multiple episodes of extensive marine anoxia linked to global warming and continental weathering following the latest Permian mass extinction. Sci. Adv. 4, e1602921.
Zhong, Y., He, B., Mundil, R., Xu, Y., 2014. CA-TIMS zircon U–Pb dating of felsic ignimbrite from the Binchuan section: Implications for the termination age of Emeishan large igneous province. Lithos 204, 14–19.
Zhou, T., Pan, X., Sun, R., Deng, C., Shen, J., Kwon, S.Y., Grasby, S.E., Xiao, J., Yin, R., 2021. Cryogenian interglacial greenhouse driven by enhanced volcanism: evidence from mercury records. Earth Planet. Sci. Lett. 564, 116902.